

CHROMOSPHERIC JET AND GROWING “LOOP” OBSERVED BY *HINODE*: NEW EVIDENCE OF FAN-SPINE MAGNETIC TOPOLOGY RESULTING FROM FLUX EMERGENCE

WEI LIU^{1,2}, THOMAS E. BERGER¹, ALAN M. TITLE¹, THEODORE D. TARBELL¹, AND B. C. LOW³

Draft version October 27, 2018

ABSTRACT

We present observations of a chromospheric jet and growing “loop” system that show new evidence of a fan-spine topology resulting from magnetic flux emergence. This event, occurring in an equatorial coronal hole on 2007 February 9, was observed by the *Hinode* Solar Optical Telescope in unprecedented detail. The predecessor of the jet is a bundle of fine material threads that extend above the chromosphere and appear to rotate about the bundle axis at $\sim 50 \text{ km s}^{-1}$ (period $\lesssim 200 \text{ s}$). These rotations or transverse oscillations propagate upward at velocities up to 786 km s^{-1} . The bundle first slowly and then rapidly swings up, with the transition occurring at the onset of an A4.9 flare. A loop expands simultaneously in these two phases (velocity: $16\text{--}135 \text{ km s}^{-1}$). Near the peak of the flare, the loop appears to rupture; simultaneous upward ejecta and mass downflows faster than free-fall appear in one of the loop legs. The material bundle then swings back in a whiplike manner and develops into a collimated jet, which is orientated along the inferred open field lines with transverse oscillations continuing at slower rates. Some material falls back along smooth streamlines, showing no more oscillations. At low altitudes, the streamlines bifurcate at presumably a magnetic null point and bypass an inferred dome, depicting an inverted-Y geometry. These streamlines closely match in space the late Ca loop and X-ray flare loop. These observations are consistent with the model that flux emergence in an open-field region leads to magnetic reconnection, forming a jet and fan-spine topology. We propose that the material bundle and collimated jet represent the *outer spine* in quasi-static and eruptive stages, respectively, and the growing loop is a 2D projection of the 3D *fan surface*.

Subject headings: Sun: activity—Sun: chromosphere—Sun: flares—Sun: magnetic topology

1. INTRODUCTION

Due to magnetic buoyancy (Parker 1955), magnetic flux ropes are expected to emerge from the convection zone into the corona through the photosphere and chromosphere. Such emerging flux regions (EFRs; Waldmeier 1937; Ellison 1944) give birth to sunspots and active regions (Weart & Zirin 1969). When observed on the solar disk, an EFR is usually seen as a new bipole in magnetograms that grows in size and magnetic flux (Zwaan 1978). The opposite polarities of the bipole separate from each other at typical velocities $\lesssim 1 \text{ km s}^{-1}$ (Harvey & Martin 1973; Chou & Wang 1987). Upflows of $\sim 1 \text{ km s}^{-1}$ at the photospheric level were observed (Brants 1985) and confirmed in recent MHD simulations (Archontis et al. 2004; Martínez-Sykora et al. 2009). Once in the low- β corona, driven by its magnetic pressure, the emerging flux expands at relatively larger velocities of $10\text{--}20 \text{ km s}^{-1}$, as observed in rising H α arch filaments (Bruzek 1967; Chou & Zirin 1988) and extreme ultraviolet (EUV) loops (Yashiro & Shibata 2000) in EFRs. Dense photospheric or chromospheric material dredged up by the emerging flux was found to consequently drain down the legs of arch filaments at $30\text{--}50 \text{ km s}^{-1}$ (Bruzek 1969; Roberts 1970). Such velocities of rise and drainage have been reproduced in MHD sim-

ulations (Archontis et al. 2004; Fan 2009).

When a flux rope emerges into an open-field region (e.g., coronal hole), magnetic reconnection between the emerging and ambient fields is expected to take place, producing a flare and material ejection (Heyvaerts et al. 1977). Such ejections were observed as *surges* in H α (Newton 1934; Roy 1973; Kurokawa & Kawai 1993) and as *jets* at other wavelengths, including white light (Wang et al. 1998), UV (Brueckner & Bartoe 1983), EUV (Alexander & Fletcher 1999), and soft X-rays (Shibata et al. 1992; Strong et al. 1992). A classification of standard and blowout jets was proposed (Moore et al. 2010). Torsional motions or helical features found in surges or jets (Xu et al. 1984; Kurokawa et al. 1987; Shimojo et al. 1996; Patsourakos et al. 2008) were interpreted as relaxation of twists from the emerging flux (Shibata & Uchida 1986; Canfield et al. 1996; Jibben & Canfield 2004). Numerical simulations have been extensively employed to explained various aspects of solar jets (Shibata & Uchida 1985; Yokoyama & Shibata 1995; Galsgaard et al. 2005; Nishizuka et al. 2008; Ding et al. 2010).

The simplest end state of flux emergence into to a (locally) unipolar region is a *fan-spine* configuration (Lau & Finn 1990; Török et al. 2009; cf., multiple nulls connected by separators, Maclean et al. 2009). As shown in Figure 1, consider a sufficiently small bipole emerging into a region of a larger scale that has a net, say, negative, flux. The emerged flux introduces two new patches of opposite polarities, with the positive patch ending up as a minority-polarity isolated in a negative polarity all around. Regardless of reconnection development, none

¹ Lockheed Martin Solar and Astrophysics Laboratory, Department ADBS, Building 252, 3251 Hanover Street, Palo Alto, CA 94304

² W. W. Hansen Experimental Physics Laboratory, Stanford University, Stanford, CA 94305

³ High Altitude Observatory, National Center for Atmospheric Research, P.O. Box 3000, Boulder, CO 80307

of the field lines from this minority patch can leave this region, because the larger, surrounding region has a net opposite flux, and thus these field lines must fountain back to the nearby photosphere. Immediately outside of this closed field is the open field, and a *dome* or *separatrix fan surface* lies in between. A magnetic *null point* is located on the top of this dome. A special open field line, the *separatrix spine*, passes through this null point to continue on into the dome interior and be rooted at the base of the atmosphere. The two parts of this spine, called the outer and inner, are identified in Figure 1. A fan-spine topology bears significant implications for solar eruptions (Antiochos 1998) and its signatures were found in anemone-like active regions (Asai et al. 2008), Eiffel tower shaped X-ray jets (Shimojo et al. 1996), saddle-like loop structures (Filippov 1999), and circular flare ribbons (Masson et al. 2009). Its presence in coronal jets or flares has been confirmed by magnetic field extrapolations (Fletcher et al. 2001; Moreno-Insertis et al. 2008) and widely reproduced in 2D or 3D MHD simulations (e.g., Yokoyama & Shibata 1996; Pariat et al. 2010).

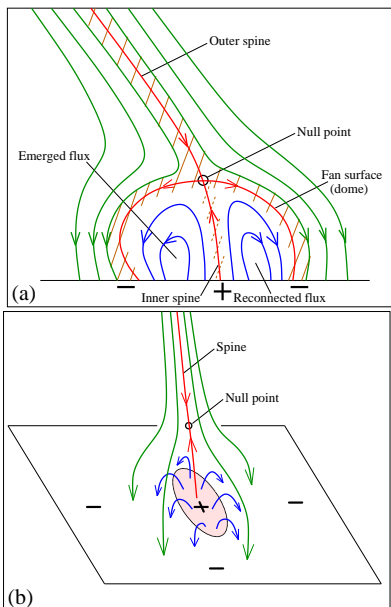


FIG. 1.— A fan-spine topology resulting from emergence of a bipole into a unipolar region: (a) 2D vertical cut; (b) 3D bird's eye view. The hatched region in (a) represents postulated bright emission (see Section 4).

The launch of the *Hinode* mission (Kosugi et al. 2007) has offered new opportunities to study the relationship and underlying physics of flux emergence, jets, and fan-spine topology in unprecedented detail (e.g.; Li et al. 2007; Shibata et al. 2007; Okamoto et al. 2008; Morita et al. 2010). In an earlier Letter (Liu et al. 2009b, hereafter Paper I), we reported an intriguing chromospheric jet observed by *Hinode* on 2007 February 9 and focused on the fine structure kinematics of the jet itself. In this paper, we present a multiwavelength study of the entire event in greater detail. In Section 2, we provide context observations, infer the unipolar magnetic environment, and investigate the associated flare. In Section 3, we pay special attention to the material bundle as the predecessor of the jet, the accompanying grow-

ing loop system, and the inverted-Y shaped geometry suggested by the streamlines of falling jet material. In Section 4, we propose that flux emergence in the unipolar region gives rise to the formation of a fan-spine topology, in which we identify the observed material bundle and jet as the outer spine and the growing loop as a 2D projection of the 3D fan surface. We conclude this paper in Section 5 and provide supplementary information in the Appendices.

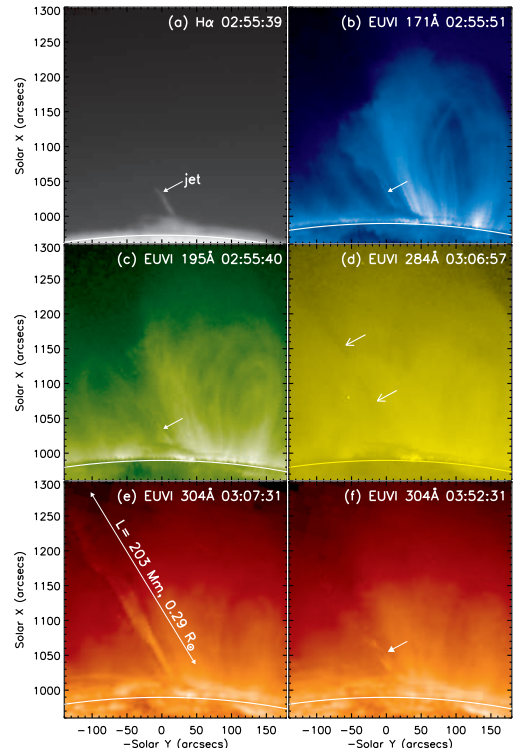


FIG. 2.— YNAO $H\alpha$ and various *STEREO* Ahead EUVI images at different stages of the event. They are rotated by 90° counter-clockwise, such that the solar north is to the left. Note the dark absorption feature of the jet material in (d) and the bright falling material in (f).

TABLE 1
EVENT MILESTONES.

02:14–02:30	earlier, brief surge-like activity
02:32	bundle of material thread appears
02:44	Ca loop and overarching SXR loop appear
02:49:02 (t_1)	onset of flare, and of fast rise of material bundle and Ca loop
02:50:32 (t_2)	end of Ca loop lateral expansion
02:51:12 (t_3)	material bundle's lower end turns from vertical rise to horizontal drift;
	Ca loop “ruptures” (apex undetectable)
02:51:44 (t_4)	elbow appears in material bundle;
	northern Ca loop leg retreats downward
02:52:24	material bundle apex starts to sweep northward
02:52:40 (t_5)	orientation angle of material bundle axis reaches maximum near flare peak; simultaneous upward ejecta and downflow in northern Ca loop leg
02:55	Ca loop leg and overarching SXR loop invisible

2. MULTIWAVELENGTH CONTEXT OBSERVATIONS

The event of interest occurred on the west limb near the equator at S03W89 from 02:14 to 04:20 UT on

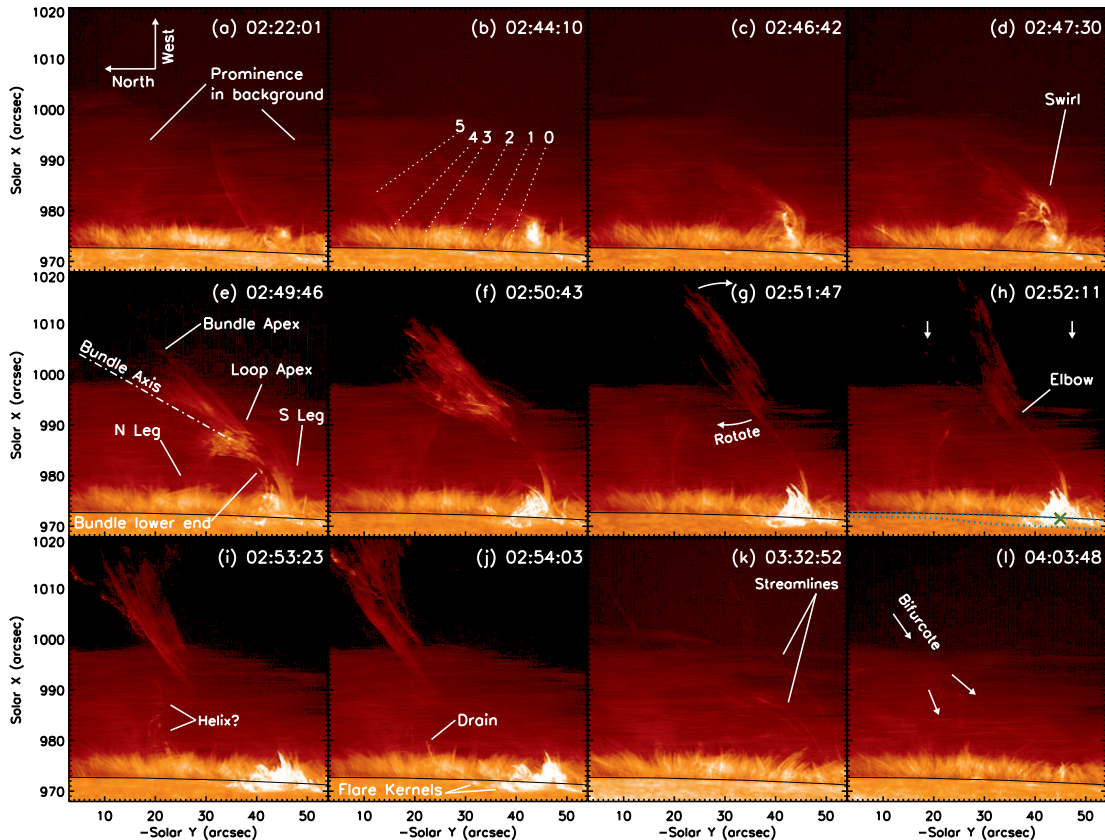


FIG. 3.— Sequence of *Hinode* Ca II H images. The numbered dotted lines in (b) represent 3'' narrow cuts perpendicular to the local threads of the material bundle. The geometric elements of the event are marked in (e). In panel (h), the cross marks the central position of the flare and the dotted line delineates the boundary of the coronal hole indicated by the PFSS model (see Figure 5); the two vertical arrows here point to the average, final solar- y positions of the loop legs since $t_2 = 02:50:32$ UT (see Figure 10(f)). Note the streamlines of the falling material in (k) and (l). (See Animation 1 in the online journal and a higher resolution version at http://www.lmsal.com/~weiliu/public/hinode/2007-02-09_sot-jet (360 MB).)

2007 February 9. This region was active in producing jets, including one at 13:20 UT on the same day (Nishizuka et al. 2008). The jet under study was observed by the *Hinode* Solar Optical Telescope (SOT; Tsuneta et al. 2008; Suematsu et al. 2008) in the Ca II H line, at a $0''.2$ spatial resolution and 8 s cadence. It was also detected in H α by the Yunnan Astronomical Observatory (YNAO; see Figure 2(a)) and a few other ground-based facilities, in EUV by *TRACE* (Handy et al. 1999), *SOHO* EIT, and *STEREO* EUV Imager (EUVI; Wuelsel et al. 2004, Figures 2(b)–(f)), and in soft X-rays (SXR) by the *Hinode* X-Ray Telescope (XRT; Golub et al. 2007). *RHESSI* (Lin et al. 2002) and XRT also observed the accompanying *GOES* A4.9 flare in X-rays. The procedure of *Hinode* SOT data reduction can be found in Paper I and details of coaligning images from various instruments are provided in Appendix A.

2.1. Overview of Ca II H, EUV, and X-ray Observations

Figures 3 and 4 show the evolution of the jet in the Ca II H line, EUV, and X-rays, and Table 1 summarizes the event time line. Early in the event, from 02:14 to 02:30 UT, there is brief surge-like activity near the limb (Figure 3(a)) and tumbling motions are seen around its base at spicule heights. At the same location, a bundle of material threads of typical width $\lesssim 1''$ appears at 02:32 UT (see online Animation 1, Figure 3(b)). This bundle, as the direct predecessor of the later jet, extends

above the chromosphere at an oblique angle toward the north and gradually swings up clockwise, seemingly unfolding itself and exhibiting oscillatory transverse motions across its axis. At the base of the bundle, a loop becomes visible at 02:44 UT and starts to expand both vertically and laterally (mainly toward the north). From 02:46 to 02:48 UT, blobs of bright emission are seen to swirl up in a helical-like trajectory from the chromosphere into the bundle (Figures 3(c)–(d)). Most of these can also be seen in *TRACE* 195 Å images (green panels in Figure 4) at lower resolution ($1''$ vs. $0''.2$ of SOT) as dark features, because the Ca II H line emission originates from partially ionized plasma at chromospheric temperatures ($\lesssim 2 \times 10^4$ K; Gouttebroze et al. 1997) that absorbs the background 195 Å emission from hot plasma at coronal temperatures (~ 1.5 MK). Some of these absorption features can be seen X-rays as well (e.g., Figure 4(f)).

Around 02:48–02:49 UT, the swing and rise of the material bundle and the expansion of the loop start to accelerate. At the same time ($t_1 = 02:49:02$ UT), the A4.9 flare sets in near the lower southern leg of the loop. It appears as bright emission in the Ca II H line (Figure 3), EUV, and X-rays (Figure 4). At $t_2 = 02:50:32$ UT, the loop legs stop their lateral expansion, and soon after ($t_3 = 02:51:12$ UT), the loop appears to rupture and its apex becomes undetectable (Figures 3(f)–(h)). At $t_5 = 02:52:40$ UT, the angle between the axis of the material bundle and the limb reaches its maximum. The

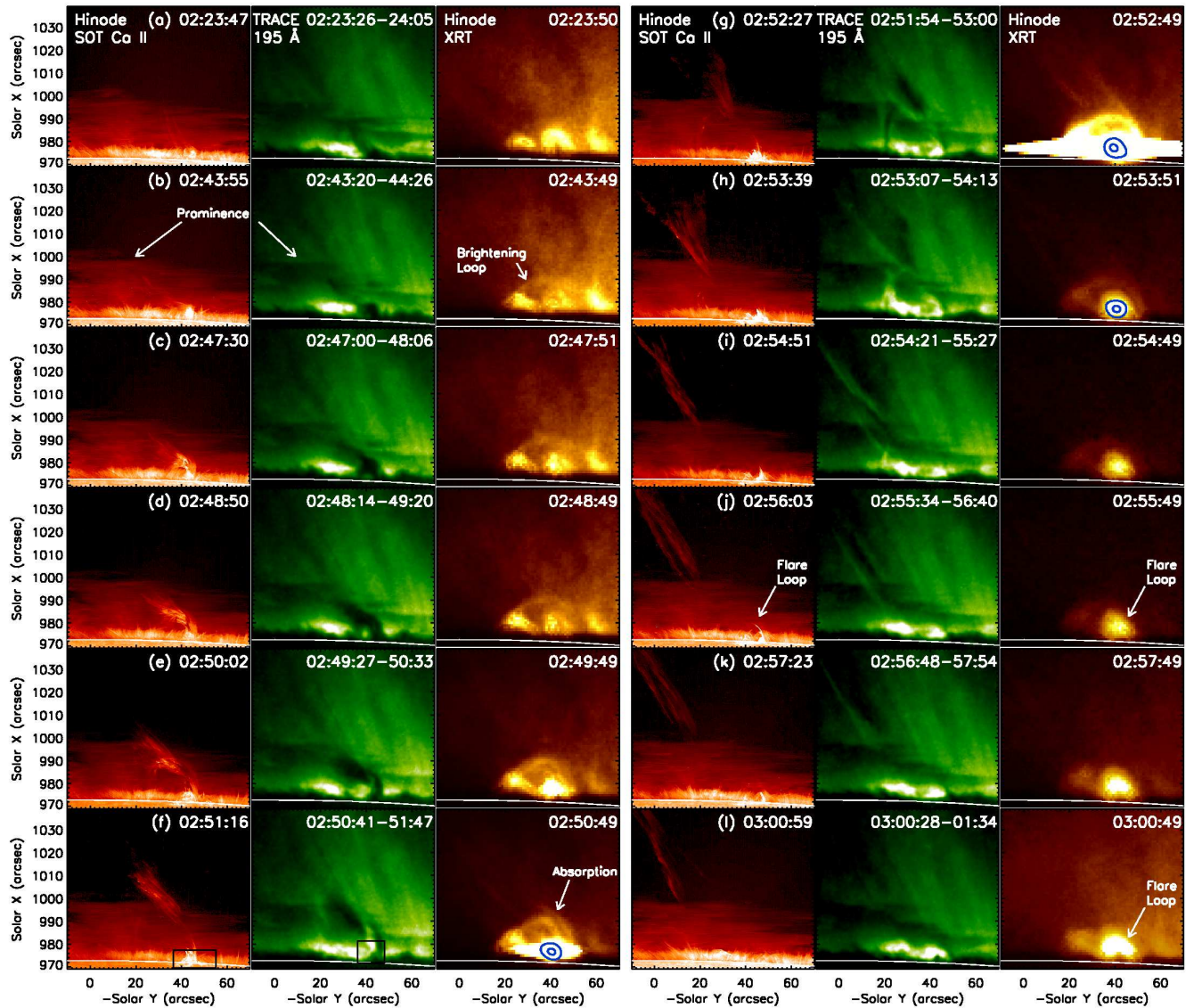


FIG. 4.— Nearly simultaneous images obtained by *Hinode* SOT in the Ca II H line (left), *TRACE* at 195 Å (middle), and *Hinode* XRT in SXR with the Al-poly or Al-poly+Ti-poly filter (right). The *Hinode* images had exposure time on the order of 1 s, while *TRACE* had long exposures as labeled. The contours at times (f)–(h) are *RHESSI* 3–6 keV images with 100 s integration centered at the corresponding XRT time. The boxes in panel (f) mark the regions for integrating source fluxes shown in Figure 7(a). (See online Animation 2.)

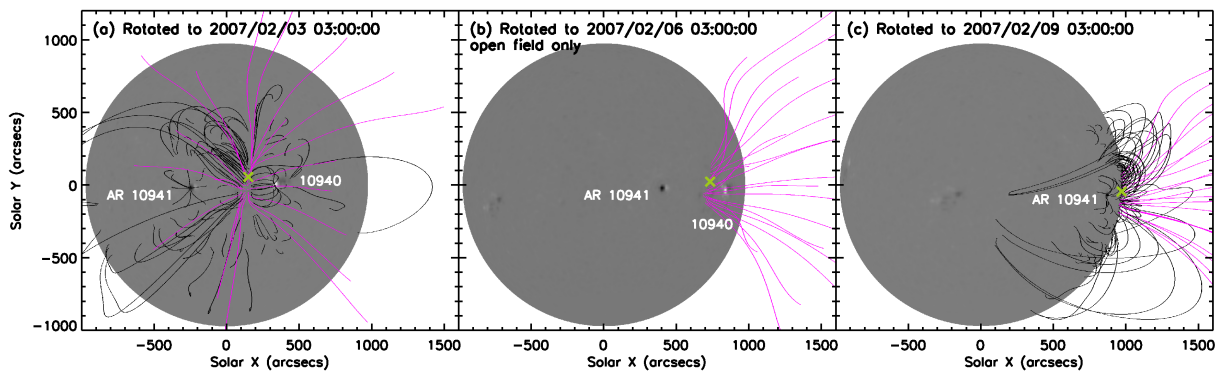


FIG. 5.— PFSS model (Schrijver & DeRosa 2003) at 00:04 UT on 2007 February 9, taken three hours before the jet. Each panel shows the global line-of-sight magnetogram and the field lines in the vicinity of the jet, as if they were seen from the Earth at the labeled time according to the Carrington rotation. Pink lines represent the open field of negative polarity, while dark lines are of the closed field. The cross sign is the same as that in Figure 3(h), marking the central position of the Ca II H flare.

bundle then starts to sweep back toward the north in a whip-like manner and rapidly develops into a collimated jet, which eventually extends to a length of 203 Mm or $0.29 R_{\odot}$ (Figure 2(e)). The loop continues to “collapse” and material is seen to drain down the northern leg toward a flare kernel only $\sim 15''$ away from the southern leg (Figures 3(i)–(j)). This indicates that the lateral expansion of the loop occurs only in the corona, while the footpoints of the loop remain anchored on the surface.

The jet material is seen as emission in the cool ($\sim 10^4$ K) Ca II H (Figure 3) and H α lines and at 304 \AA ($\sim 10^5$ K) and 171 \AA (~ 1 MK), as absorption in the hotter (~ 2 MK) 284 \AA line (Figure 2), as multiple strands of absorption and emission at intermediate (~ 1.5 MK) 195 \AA (Figure 4), and as weak emission in XRT SXR (~ 1 – 30 MK; Figure 4(g)). This indicates a wide range of temperatures, from 10^4 to 10^6 K, in the jet plasma. The jet exhibits oscillatory transverse motions across its axis as seen by SOT, which we interpreted in Paper I as spins resulting from unwinding twists. Further evidence of this interpretation is found at 195 \AA , where the emission and absorption strands alternate and shadow each other in sequence, as expected for a spinning cylinder in a side view (see online Animation 2).

Later in the event, a flare loop appears in SXR and then EUV (Figure 4). Part of the jet material that fails to escape the gravitational bound returns to the chromosphere along smooth streamlines in the original direction of ascent (Figure 2(f)). The oscillatory transverse motions seen earlier in the jet are no longer present in the falling material (see Figures 1 and 3 in Paper I). At lower altitudes, most of the streamlines bypass a dome-shaped region and outline an inverted-Y geometry (Figure 3(k)).

2.2. Magnetic Environment: Local Coronal Hole

This event occurred near the limb and thus there was no reliable direct magnetic field measurement available. We then resorted to the potential field source surface (PFSS) model (Zhao & Hoeksema 1994; Schrijver & DeRosa 2003) available in the *Solar SoftWare* package to obtain indirect information of the magnetic topology in the vicinity of the jet. The modeled field is the extrapolation of a photospheric magnetogram that combines *SOHO* MDI observations within 60° of the disk center and the evolved fields elsewhere according to the flux disperse model.

Figure 5 shows the PFSS model field at 00:04 UT near the time of the event, as seen from different view angles. We noticed a north-south oriented narrow channel (range: 6° in longitude, 18° in latitude) of open field or a *coronal hole* located between two NOAA active regions (ARs) 10940 and 10941. The models up to seven days prior to the event show that this coronal hole persistently existed, evolved slowly in size and shape, and matched the dark regions seen in *SOHO* EIT 284 \AA images as expected.⁴ We then rotated the 00:04 UT model field to the time of the jet according to the Carrington rotation rate, and found that the event was located inside the coronal hole. An example is shown in Figure 3(h),

⁴ See the model predicted coronal hole boundaries at <http://www.lmsal.com/isolsearch> and their overlays on EIT images at <http://lmsal.com/forecast/modelEUV>.

where the coronal hole boundary (dotted line) encompasses the kernels of the flare. This is consistent with the finding of Nitta et al. (2008) for an active region jet and with the expectation that coronal jets tend to occur in open-field regions, as manifested by the ubiquitous polar jets observed by *Hinode* (Cirtain et al. 2007; Shibata et al. 2007). Close comparison with the PFSS model further indicates that the north-west orientation of the jet is close to those of the open field lines, again as expected from classical jet models. This can be clearly seen in both SOT Ca II H and *STEREO* 304 \AA images (Figure 6).

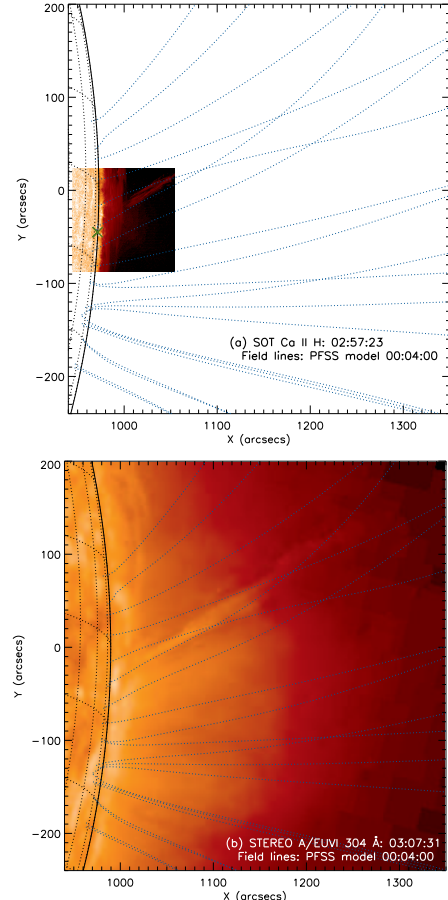


FIG. 6.— Open field lines of the PFSS model (as shown in Figure 5) overlaid on (a) the SOT image from Figure 4(k) and (b) the *STEREO* Ahead 304 \AA image from Figure 2(e). The field lines were projected according to the positions of the corresponding spacecraft at the times of the images. The cross sign in (a) is the same as that in Figure 3(h).

2.3. Associated Microflare

The accompanying A4.9 flare occurred at 02:49 UT and peaked at 02:53 UT in the *GOES* low channel (1 – 8 \AA) flux. As can be seen in Figures 7(a)–(c), the light curves in the Ca II H line (SOT) and X-rays (*GOES* and *RHESSI*) are very similar, showing a single hump, except for slightly different onset and peak times, presumably due to different instrument response to the varying plasma temperature. The *TRACE* EUV light curve shows a different trend except during the rise of the flare.

The initial decrease from 02:37 to 02:47 UT is due to the unfolding material bundle and growing loop at chromospheric temperatures, which lead to increased absorption of the background EUV emission. The second flux increase (02:56–03:01 UT) is likely the result of the hot X-ray emitting plasma cooling to 195 Å passband temperatures and/or continuous evaporation of chromospheric plasma due to thermal conduction (Zarro & Lemen 1988; Battaglia et al. 2009; Liu et al. 2009d).

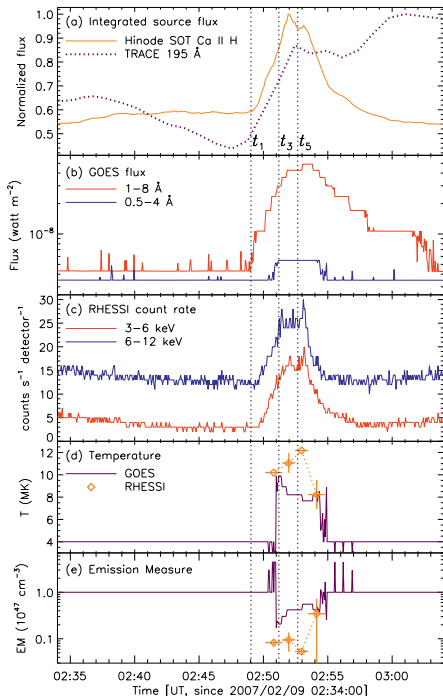


FIG. 7.— Time line of the accompanying flare. (a) Normalized *Hinode* Ca II H and *TRACE* 195 Å fluxes integrated over the source regions boxed in Figure 4(f). (b) and (c) *GOES* and *RHESSI* X-ray light curves. (d) and (e) Temperature and emission measure obtained from *GOES* and *RHESSI*.

The flare emission appears near the lower southern leg of the loop and cospatial at various wavelengths, from Ca II H to EUV and X-rays (Figures 3 and 4). It is seen by *RHESSI* up to the 6–12 keV band. Fits to *RHESSI* spectra at the flare peak indicate that the emission is primarily thermal bremsstrahlung from a plasma of temperature $T = 12.2 \pm 0.6$ MK and emission measure $EM = (5.3 \pm 0.5) \times 10^{45} \text{ cm}^{-3}$ (see Appendix B). As shown in Figures 7(d) and (e), T and EM have simple temporal profiles. Their differences between *GOES* and *RHESSI* likely result from the well-known fact that *GOES* is more sensitive to cooler plasmas. Note that, because of their sharp occultation at the chromospheric limb, the three bright loops seen earlier by XRT (Figure 4(a)) are most likely located in AR 10940 behind the limb, together with those large-scale EUV loops seen in Figure 2. The flare loop happens to be in front of the background loop in the middle ($y \sim -40''$) and is located on the visible side of the disk, since its footpoints are inside the limb (Figure 4(l)) and the flare kernels are clearly observed (Figure 3(j)).

3. *Hinode* SOT DATA ANALYSIS

In this section, we make geometric measurements of various features projected onto the sky plane observed by *Hinode* SOT in the Ca II H line. Bear in mind that projection effects may limit our capability of uncovering the true 3D picture. Here we assume that the displacements of Ca emission features represent motions of material rather than sequential excitations of emission due to temperature or density variations (see Appendix C).

3.1. Material Bundle: Jet Predecessor and Early Development

As briefly mentioned in Section 2.1, the predecessor of the jet is a bundle of material threads that exhibits transverse motions across its axis. To quantify these motions, we have placed six $3''$ wide cuts along the bundle, oriented roughly perpendicular to the local threads as shown in Figure 3(b). Space-time diagrams (Figure 8) of these cuts clearly show oscillatory transverse motions between 02:36 and 02:48 UT, particularly in the upper portion of the bundle (Cuts 2–5). We selected Cut 3 as an example and fitted those unambiguously identified piecewise tracks with a sine function of time t :

$$s_{\perp}(t) = s_{\perp 0} + A \sin \left[\frac{2\pi(t - t_0)}{P} \right], \quad (1)$$

where s_{\perp} is the distance along the cut (\perp to threads), A the amplitude, and P the period. The resulting fits are shown in Figure 9. Compared with those in the late stage of the jet as shown in Figure 4 of Paper I, the oscillation velocities ($v_{\perp} \sim 50 \text{ km s}^{-1}$) at the equilibrium position here are about 1.5–2 times larger, while the amplitudes and periods are smaller by similar fractions.⁵

To track the propagation of these oscillations, we identified the crests of an oscillation in Cuts 2–5 as marked by the plus signs on the left in Figure 8, which exhibit a delay from one cut to the next. We then fitted the separations of the cuts vs. the occurrence times of the crests with a linear function. (Here the cut separations are defined as the distance from the center of the cut to the previous neighboring cut.) This yields a speed of $v_{\text{ph}} = 786 \pm 30 \text{ km s}^{-1}$ for the upward propagation, which is formally identified as a phase speed here. This speed is similar to its later counterpart at the leading edge of the jet (see Figure 3 of Paper I). If these oscillations are MHD waves, the wavelength would be $\lambda = v_{\text{ph}} P = v_{\text{ph}}(192 \pm 12 \text{ s}) = 151 \pm 11 \text{ Mm}$. We also located the onset (marked by crosses) of the rapid rise of the bundle in each cut. A parabolic fit indicates an acceleration of $a = 4.6 \pm 0.5 \text{ km s}^{-2}$ and a final speed of $v_{\text{ph}} = 401 \pm 39 \text{ km s}^{-1}$ at the highest Cut 5.

Next, we quantify the rise of the material bundle by tracking its apex, lower end, and axis as marked in Figure 3(e). The apex and lower end are identified as the highest and lowest point in altitude of the ensemble of the bundle threads, respectively. The axis is recognized as the bisector of the bundle’s angular extent and is characterized by its orientation angle θ_{bdl} from the limb. Figures 10 shows the history of these geometric parameters,

⁵ The amplitudes and periods might have been underestimated here, because each fit was done for less than a full cycle due to ambiguities and the changing brightness of material threads. However, the instantaneous oscillation velocities are not affected.

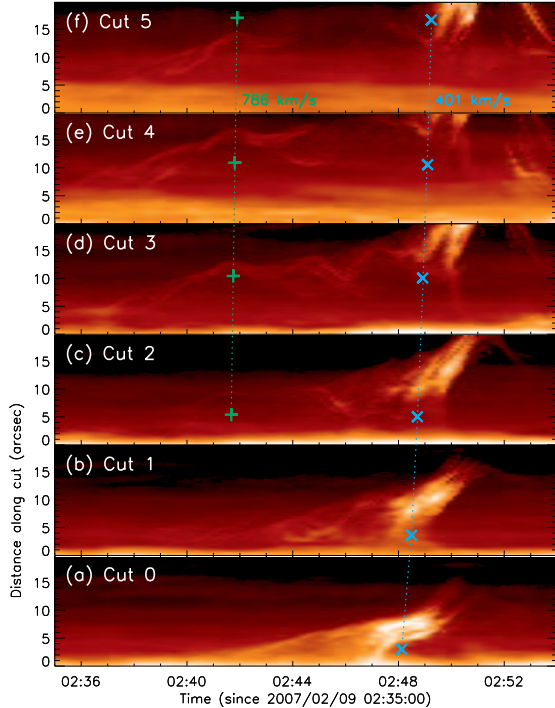


FIG. 8.— Space-time plot of cuts perpendicular to the local threads of the material bundle as shown in Figure 3(b). The plus signs indicate the times of the crest of a sinusoidal oscillation, and the crosses mark the onsets of the rapid rise of the bundle, both indicating a delay at higher cuts. The vertical positions of the symbols are scaled with the separations of the corresponding cuts and are fitted with the dotted lines (see text) labeled by their final velocities. (See the original images overlaid with the cuts in online Animation 3.)

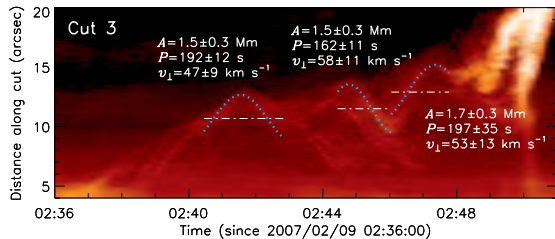


FIG. 9.— Same as Figure 8(d) but with an enlarged view and slightly different color scale to emphasize oscillatory tracks. Overlaid are sinusoidal fits (thick dotted line) to selected tracks, and listed nearby are the fitted parameters: amplitude A , period P , and velocity v_{\perp} at the equilibrium position marked by the dot-dashed line.

which, together with those shown in Figure 12, are fitted with a piece-wise linear and/or parabolic function of time, depending on their temporal evolution, to infer their velocities and/or accelerations.

We find a **slow-to-fast two-phase** evolution clearly divided by the onset of the accompanying flare at $t_1 = 02:49:02$ UT. (1) Prior to t_1 , the apex height h_{bdl} , axis angle θ_{bdl} , and displacements of the bundle's lower end from its initial position (Δx_{bdl} , Δy_{bdl}) show *slow* variations (Figures 10(b)–(d)). The clockwise upward swing of the axis is evident in the increase of θ_{bdl} at a moderate velocity of $\dot{\theta}_{\text{bdl}} = (4.9 \pm 0.2) \times 10^{-2} \text{ deg s}^{-1}$. (2) At the flare onset, all of these quantities but Δy_{bdl} start to increase *rapidly*. $\dot{\theta}_{\text{bdl}}$ experiences an acceleration and reaches $(3.1 \pm 0.2) \times 10^{-1} \text{ deg s}^{-1}$ at $t_5 = 02:52:40$ UT

when its growth comes to a stop followed by a reverse. Overall, θ_{bdl} has gained more than 50° in 10 minutes. The bundle's lower end first moves mainly upward (Δx_{bdl}) with an acceleration of $0.66 \pm 0.09 \text{ km s}^{-2}$ (final velocity: $110 \pm 6 \text{ km s}^{-1}$). At $t_3 = 02:51:12$ UT, it **turns** to a primarily horizontal direction (Δy_{bdl} , *northward*) with a comparable acceleration and slight decrease in height by $3''$ (Figures 10(d) and 13(c)). At the same time, the top portion of the bundle continues swinging up and *southward*.⁶ This makes the bundle rotate clockwise, forming an **elbow** or bend toward the north at $t_4 = 02:51:44$ UT (Figures 3(g) and (h)). Soon after this (02:52:24 UT), the *entire* material bundle quickly sweeps toward the *north* like a whip, developing into a collimated jet, and individual threads stretch upward as fast as $176 \pm 11 \text{ km s}^{-1}$ (Figure 10(b)).

3.2. Accompanying Growing Loop

Another key component of this event is the growing Ca II H loop that accompanies the rise and eruption of the material bundle. We track the evolution of its apex height h_{loop} and the lateral span of its two legs (Figures 3(e)). The latter is derived from the solar- y coordinates of the legs' outer edges since the y -axis here near the equator is almost parallel to the limb.

Similar to the material bundle, the loop apex also experiences two distinct phases divided at the flare onset t_1 (Figure 10(e)): (1) a **gradual phase** from 02:44 to t_1 with a moderate ascent velocity of $16.2 \pm 0.4 \text{ km s}^{-1}$ and (2) an **acceleration phase** from t_1 to $t_3 = 02:51:12$ UT with an acceleration of $0.73 \pm 0.06 \text{ km s}^{-2}$ and a final velocity of $135 \pm 4 \text{ km s}^{-1}$. The second phase ends when the loop appears to rupture and its apex is no longer visible. This coincides with the turning point of the material bundle's lower end mentioned above (Figure 10(d)). Similar phases of slow and fast rises have also been reported in other eruptive events, including coronal jets (Patsourakos et al. 2008) and prominence eruptions (Sterling & Moore 2005; Chifor et al. 2006; Liu et al. 2009e).

The lateral position y_{NLeg} of the northern leg of the loop has a similar two-phase evolution with 1–2 times larger velocities and acceleration (Figure 10(f)). In contrast, the southern leg does not show such a distinction and has a uniform low velocity of $5.2 \pm 0.1 \text{ km s}^{-1}$, only $\frac{1}{4}$ of its northern counterpart ($23.3 \pm 0.7 \text{ km s}^{-1}$) in the gradual phase. This **asymmetry** means that the lateral expansion of the loop is primarily on the northern leg moving toward the north. Note that the lateral expansion velocity and acceleration averaged between the two legs roughly equal their vertical counterparts. The lateral expansion, however, ceases *earlier* than the vertical growth. This occurs in both legs at $t_2 = 02:50:32$ UT $< t_3$, after which they remain stationary with small fluctuations (standard deviation: $0''.4$).

To examine the shape of the loop, we define the aspect ratio of the loop apex height to the half separation of the two legs in the north-south direction, $R \equiv h_{\text{loop}} / [(y_{\text{NLeg}} - y_{\text{SLeg}}) / 2]$. As shown in Figure 10(g), this ratio has a mean of $2.2 > 1$, indicating vertical elongation.

⁶ The bundle's apex height does not appear to increase monotonically, because of the jumps caused by changes in brightness and thus switches of the feature to be tracked (Figure 10(b)).

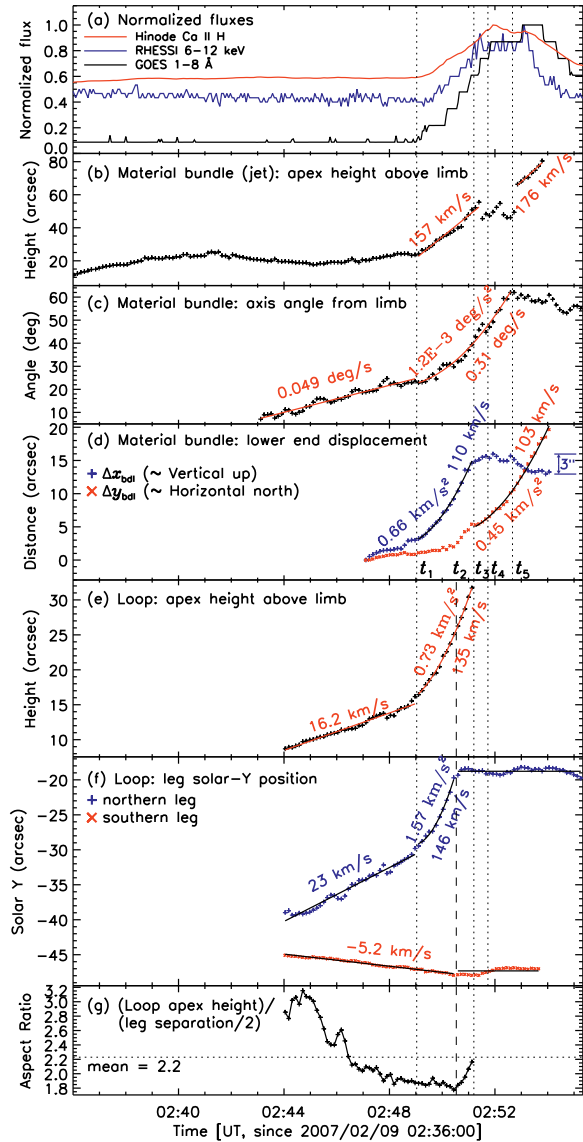


FIG. 10.— History of geometric quantities of the Ca II H material bundle (jet) and loop. (a) Light curves at various wavelengths repeated from Figure 7. (b) Height h_{bdl} of the material bundle apex. (c) Angle θ_{bdl} of the material bundle axis from the horizon. (d) Solar x and y displacements of the lower end of the material bundle as shown in Figure 13(c). Major milestones of the event are labeled as t_1, \dots, t_5 . (e) Height h_{loop} of the loop apex. (f) Solar- y coordinates of the northern and southern legs of the loop, y_{NLeg} and y_{SLeg} . The horizontal lines starting at $t_2 = 02:50:32$ UT mark the means of the data after this time. Velocities and accelerations from linear and parabolic fits are labeled in (b)–(f). (g) Aspect ratio of the loop apex height h_{loop} to the half separation of the two legs in the north-south direction, $(y_{\text{NLeg}} - y_{\text{SLeg}})/2$.

gation. The elongation is reduced with R decreasing from ~ 3.2 to 1.8 during the gradual expansion phase (02:44 UT– t_1). The loop then preserves its shape with a constant aspect ratio ~ 1.8 during the common acceleration phase (t_1 – t_2), but the elongation slightly increases afterward because of the earlier cessation of the lateral expansion.

Near the end of the visible lifetime of the accompanying loop, the northern leg exhibits interesting behaviors. There are two branches at this leg which initially expand upward during the loop growth. When the el-

TABLE 2
FITTED VELOCITIES AND ACCELERATIONS OF BLOBS IN THE NORTHERN LEG OF THE LOOP AT ITS LATE STAGE

trajectory or blob ID	linear fit	parabolic fit	
	$\langle v \rangle$ (km s^{-1})	a/g_{\odot}	v_{final} (km s^{-1})
A	-94 ± 5
B	121 ± 5	11.4 ± 3.1	192 ± 18
C	58 ± 5	11.1 ± 2.6	130 ± 18
D	-95 ± 4
E	-57 ± 2	-4.8 ± 0.7	-115 ± 9

bow of the material bundle appears at $t_4 = 02:51:44$ UT as noted above, the two branches start to bend and retreat downward. We identified five bright blobs (A–E) as shown in Figure 11, among which blobs A and D represent the visible apices of the two branches. We then tracked the blob locations with time (Figure 12(a)) and used blob sizes as uncertainties. For each blob, its positions are well represented by a straight line fit, which gives its main direction of motion. We obtained the distance along this direction and inferred the corresponding velocity and/or acceleration (Figures 12(b) and (c)).

We find that both blobs A and D exhibit a downward acceleration followed by a deceleration within ~ 1 minute, and their average velocities are nearly -100 km s^{-1} (see Table 2). Near the onset (02:52:24 UT) of the northward sweep of the material bundle, blob A becomes too vague to be identified, while two new blobs, B and C, appear nearby. They shoot upward with an acceleration $a \sim 11g_{\odot}$ (where $g_{\odot} = 0.274 \text{ km s}^{-2}$ is the solar gravitational constant) and reach final velocities of 192 ± 18 and $130 \pm 18 \text{ km s}^{-1}$. In contrast, as blob D slows down its downfall near $t_5 = 02:52:40$ UT, it turns its horizontal direction from the north to the south (Figure 12(a)) and we assign it a new blob ID named E. This blob resumes a downfall with an acceleration of $a = (-4.8 \pm 0.7)g_{\odot}$ and reaches a velocity of $-115 \pm 9 \text{ km s}^{-1}$ just before it plunges into spicules in the chromosphere. Since the blobs are tracked by their projected 2D positions in the sky plane, these velocities and accelerations are lower limits of their true values in 3D space. Meanwhile, the solar gravitational acceleration g_{\odot} is the upper limit of its component along the unknown 3D trajectory. Thus blob E’s downward acceleration is at least 5-fold greater than a corresponding free-fall (dotted line in Figures 12(b)). Its final velocity is also 2–3 times larger than those (30–50 km s^{-1}) found at the footpoints of $H\alpha$ arch filaments (Bruzek 1969; Roberts 1970). Even if a free-fall starts at a higher altitude at the top of trajectory D, it would reach a final velocity of only 42 km s^{-1} , about $\frac{1}{3}$ of trajectory E’s value.

3.3. Streamlines of Falling Material: Inverted-Y Geometry

As mentioned earlier, jet material bound by gravity falls back to the chromosphere and this continues throughout the duration of this event. The trajectories of the falling material are smooth streamlines, which, at altitudes $\gtrsim 20''$, are almost straight lines in the original direction of ascent. Kinematics of the falling material above this height was investigated in Paper I using space-time plots (see Figure 2 there). Below this height, the streamlines are curved as if they bypass an unseen dome or null point. This can be clearly seen in the online Animation 1, especially from 03:25 to 03:35 UT.

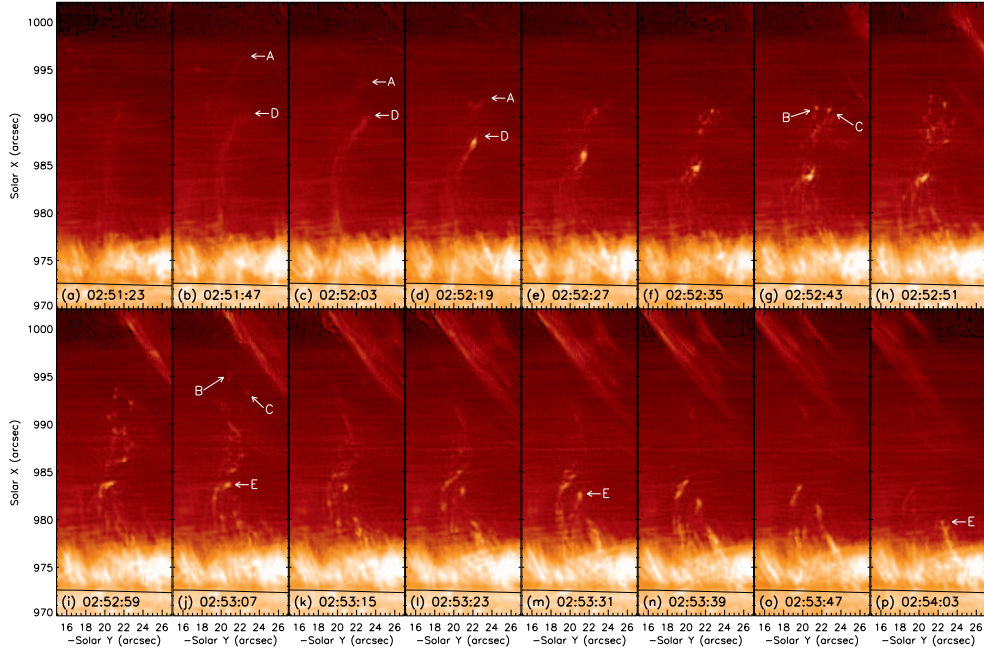


FIG. 11.— Enlarged view of the northern leg of the Ca II H loop at its late stage. Note the downward retreat of branches A and D and the upward ejection of blobs B and C.

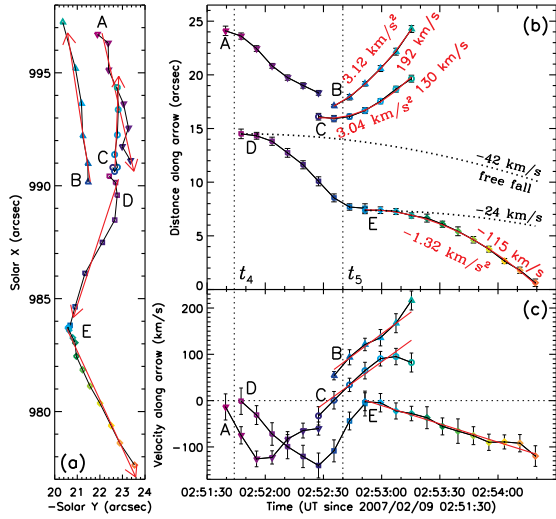


FIG. 12.— Kinematics of the emission blobs in the northern leg of the loop as marked in Figure 11. (a) Locations of blobs A–E with colors from magenta to red indicating time evolution. For each blob, a red arrow represents the main direction of motion, given by a linear fit to the data. (b) Distance along the main direction of motion for each individual blob, with positive (negative) for upward (downward). The curves are shifted vertically to make their end points approximately represent the relative heights of the corresponding blobs. (c) Time derivative of the distance in (b). The red lines in (b) are parabolic fits to curves B, C, and E, labeled with the fitted accelerations and final velocities, and their counterparts in (c) are the corresponding velocities vs. time.

To highlight these streamlines, we performed running difference between each pair of images 2 minutes apart (every 15 frames at an 8 s cadence) within a selected duration, and superimposed the positive parts of all differenced images. A sample of the results is shown in Figures 13(a)–(c). We then visually traced the streamlines, a collection of which clearly outlines an inverted-Y geometry (Figure 13(d)). By overlaying these streamlines on top of multiwavelength images (Figures 13(e)–

(h)), we note the following spatial relationships: (1) some streamlines, particularly those on the right-hand side, are distributed close to the growing Ca loop at its final stage; (2) the inverted-Y goes around the cusp-shaped flare loop seen in SXR; and (3) three branches (labeled b_0 , c_1 , and a_1) of the streamlines are cospatial with the dark absorption features seen in EUV, which likely represent the same cool material that emits in Ca II H. We also note that the drift of the material bundle’s lower end terminates at 02:54 UT near the bifurcation of the streamlines 1 hr later (Figures 3(l) and 13(c)).

4. INTERPRETATION OF OBSERVATIONS

The observations presented above bear two significant implications. First, the Ca loop comes into sight on the visible side of the limb, starts to grow into the chromosphere among neighboring spicules, and makes its way into the corona, expanding vertically and laterally. This suggests that the growing loop results from the **emergence** of a magnetic bipole from below the photosphere. This inference is supported by the following three factors: (1) The loop’s initial upward expansion velocity of $16.2 \pm 0.4 \text{ km s}^{-1}$ is of the same order of magnitude as the $10\text{--}15 \text{ km s}^{-1}$ Doppler velocities of rising arch filaments in EFRs (Chou & Zirin 1988), as well as the $\sim 20 \text{ km s}^{-1}$ speeds of emerging flux ropes found in 3D MHD simulations (Archontis et al. 2004; Fan 2009; Martínez-Sykora et al. 2009) and of recently discovered prominence plumes (Berger et al. 2008). (2) The separation ($\lesssim 15''$) of the flare kernels (at loop footpoints) is only $\frac{1}{2}$ of the separation between the Ca loop legs, which is expected for emerging flux due to its rapid lateral expansion in the corona. (3) In addition, it is possible that the earlier, weaker surge⁷ (02:14–02:30 UT) is the initial

⁷ This earlier surge and the main jet, together with another jet occurring 10 hrs later (Nishizuka et al. 2008), could be

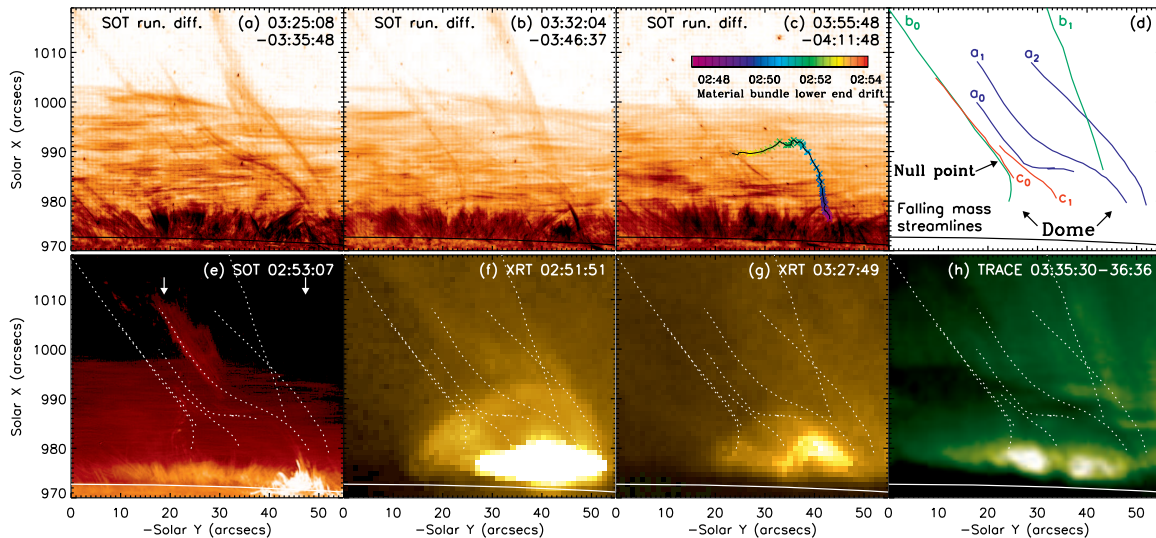


FIG. 13.— (a)–(c) Stacked running difference images showing streamlines of the falling material in three time intervals. (d) Streamlines obtained from panels (a)–(c) in different colors as labeled. (e)–(h) *Hinode* SOT Ca II H, XRT, and *TRACE* 195 Å images at various stages of the event, overlaid with the same streamlines shown in (d). The colored symbols in (c) represent the temporal migration of the lower end of the material bundle (see Section 3.1), presumably near the null point. The two vertical arrows in (e) are the repetition from Figure 3(h).

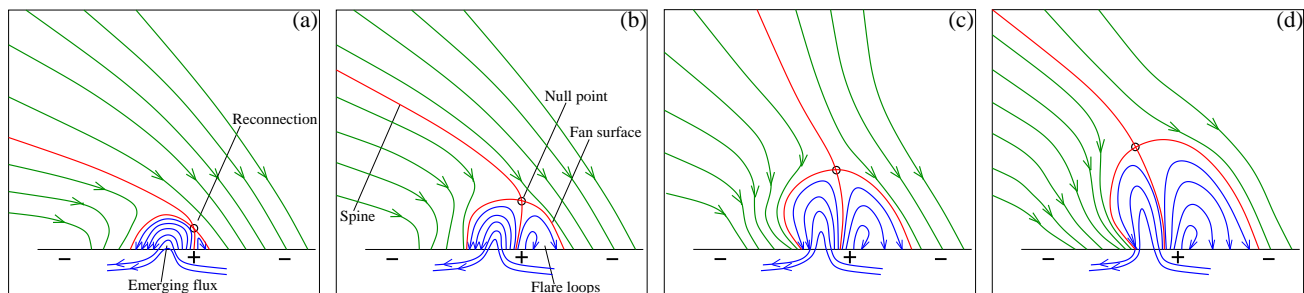


FIG. 14.— A 2D cut of the proposed model for the event development, indicating magnetic reconnection between the emerging flux and ambient field. The green field lines represent the unipolar surrounding field, the blue lines represent the closed field underneath the separatrix fan surface (dome), and the red lines represent the dome and spine. Beneath the dome, the emerging flux is located to the left of the inner spine and the newly reconnected flux is to the right. Note the preferentially northward (toward the left) expansion of the fan surface, the changing orientation of the spine, and the migration of the null point from one magnetic flux surface to another as the result of reconnection. This is a simplified 2D rendition of the true 3D configuration with topological quasi-axisymmetry about the spine (as shown in Figure 1(b)) and can be readily compared with our 2D observations. In a 3D case (e.g., see figures in Pariat et al. 2009, 2010), there are twists in the field and both sides of the spine are within a single topologically connected domain.

signature of flux emergence. If so, the 30 minutes delay of the first appearance of the Ca loop at 02:44 UT is consistent with the time scale for the emergence of a typical small-scale ephemeral region. This time is required for the emerging flux to be built up in order to generate sufficient upward pressure force and to drain heavy material carried from the interior before it can further expand into the corona.

We note that, other than flux emergence, footpoint shearing, twisting, or braiding motions of a *pre-existing* coronal structure, such as an arcade of coronal loops, can also increase its magnetic stress and helicity and cause it to expand or even erupt (e.g., Antiochos et al. 1999; Rachmeler et al. 2010). So we examined available data from *Hinode*, *TRACE*, and *STEREO*. However, we found no indication (either emission or absorption) of the prior existence of the loop or material bundle at any size resolved by the instruments (down to $0''.2$) and up

part of the recurring jet activity, which has been observed in other events (Chifor et al. 2008) and simulated with MHD models (Archontis et al. 2010; Pariat et al. 2010).

to two hours before this event. These data include multiple wavelengths — Ca II H, EUV (171, 195, 284, and 304 Å), and soft X-rays — which cover a wide range of temperatures (10^4 – 10^7 K). This essentially rules out the possibility that the appearance of the Ca loop results from temperature changes and/or expansion of a pre-existing coronal structure. Hence, flux emergence still remains the most likely possibility for the origin of the Ca loop, although we have no reliable magnetograms of this near-limb region to provide direct evidence.

The second implication of our observations is that, as mentioned in Section 1, any bipole emerging into a unipolar region, i.e., the coronal hole in this case, can naturally lead to a **fan-spine** topology (Antiochos 1998; Török et al. 2009). The streamlines of the falling material, assumed to be parallel to magnetic field lines, clearly indicate such a configuration as shown in Figure 1. In particular, streamlines a_0 and b_0 evidently bifurcate, suggesting that the spine is located between them and the null point lies close to the bifurcation. The fact that the streamlines avoid the dome indicates that the jet material originates from above the separatrix fan surface.

There are, however, outliers to this general trend, and streamlines b_1 and c_1 apparently pass through the dome. This is likely a projection effect of the true 3D geometry, in which these streamlines lie behind or in front of the dome that has a finite extent along the line of sight (e.g., Figure 1(b)).

Note that the 3D fan-spine configuration has a variant form in a 2D geometry with translational invariance in the third dimension or in a 3D geometry with a significantly elongated parasitic polarity. In this case, the *3D null point* is replaced with a *separator line* and the spine line is replaced with a spine surface. This surface divides the volume underneath the dome into two topologically separate chambers (see Figure 3 of Moreno-Insertis et al. 2008), which are, however, a single connectivity domain in the true 3D null case. The observations of flow streamlines very likely located behind or in front of the inferred dome provide a basis for our adoption of the true 3D null model for our discussion in the rest of the paper.

4.1. Proposed Model

Based on the above two inferences, we postulate that the earlier *material bundle* and later *collimated jet* represent the *outer spine* and its neighboring field lines in different stages, while the *growing Ca loop* is a 2D rendering (projection) of the entire 3D *dome or separatrix fan surface* (Figure 1). We believe that, among alternative models, this conjecture best explains the observations. The postulated event develops as follows (see Figure 14).

When a twisted flux rope emerges into the corona in an open-field environment, the flux rope expands rapidly, driven by its considerable magnetic pressure, and presses onto the ambient field to form a current sheet at the discontinuity between them (Heyvaerts et al. 1977). Magnetic reconnection ensues and results in a fan-spine structure mentioned above. The outer spine originates from the null point and opens to infinity, while the inner spine apparently divides the vault under the dome into two parts seen in 2D projection.

Reconnection outflows continuously pump dense plasma upward along the newly reconnected field lines near the **outer spine**. Emission from such plasma (hatched region around the spine in Figure 1(a)) could be responsible for the observed **material bundle** and later **collimated jet**, whose diffuse upper end and relatively sharp lower end (Figures 3(f)–(h)) are readily explained by the geometry of the outer spine. Reconnection also transfers magnetic helicity from the emerging flux rope into the newly reconnected open field. This and plasma pumping are both manifested in the upward swirling motion of material along the helical trajectory observed around 02:47 UT (Figures 3(c)–(d)). Under the influence of the Lorentz force, the twists in the reconnected open field tend to unwind themselves and drive these field lines to rotate, as found in spinning $H\alpha$ surges (Shibata & Uchida 1986; Canfield et al. 1996). Such spins propagate up toward the open end in the form of torsional MHD waves, and their 2D projections would appear as traveling sinusoidal oscillations, just as observed here (Section 3.1). The inferred rotational velocities and periods (Figure 9) are comparable to those of transverse oscillations found in X-ray jets (Cirtain et al. 2007), prominences (Okamoto et al. 2007), and coronal loops (Ofman & Wang 2008), which were interpreted as

signatures of Alfvén or fast kink mode waves. Our inferred phase speed of $v_{\text{ph}} = 786 \pm 30 \text{ km s}^{-1}$ is also within the range of typical coronal Alfvén or fast-mode speeds. At the same time, the Lorentz force associated with the twists and axial gradient of currents (e.g., see the current density in Figure 9 of Pariat et al. 2009) may have a strong axial component that can drive the upward ejection of material along the axis of the bundle (Bellan et al. 2005).

As the dense emerging flux rope expands and sweeps through the dense lower atmosphere ahead of it, a layer of enhanced local density is expected to form at its leading front. In our case, this layer is the **fan surface** between the emerging flux and the ambient open field, marked as the hatched region on the dome in Figure 1(a). In 2D projection, it could appear as the **growing Ca loop** seen here. The expansion rate of the flux rope, presumably depending on the flux emergence rate and the interplay between the strengths of the emerging field and the surrounding field, controls the dynamic evolution. Early in the event (before $t_1=02:49:02$ UT), the flux rope (thus the fan surface) expands at a moderate speed ($16.2 \pm 0.4 \text{ km s}^{-1}$), giving the ambient field a *gentle* push. This leads to moderate rates of reconnection and supply of mass and helicity to the *material bundle* around the spine, which evolves in a quasi-static manner. As sufficient twists have emerged into the corona with time, a kink-like instability can occur and force the flux rope to undergo an accelerating expansion (Fan & Gibson 2004; Pariat et al. 2009; Rachmeler et al. 2010), *strongly* pushing the ambient field and thus driving rapid reconnection. If we interpret flares to be indicators of rapid energy release by fast reconnection, we may identify time t_1 as the onset of the observed flare heating in this event. In addition, the increased fluxes of mass and helicity transferred to the material bundle through reconnection can no longer relax in a quasi-static manner, eventually resulting in a runaway instability that leads to the *collimated jet*. This explains the simultaneous transitions from **slow to fast evolution** for both the material bundle and growing loop (Figure 10). This is also energetically analogous to the two regimes found by (Pariat et al. 2010): slow, quasi-static reconnection in the energy-storage phase and fast, dynamic reconnection in the energy-release phase in a rotating current sheet associated with the kinking flux under the fan surface.

Because of continuous reconnection, the material bundle around the spine is a constantly **evolving entity**. A given field line in the bundle is illuminated only when reconnection drives dense mass flow along it. It becomes invisible once the temperature leaves the Ca II H response range ($\lesssim 2 \times 10^4 \text{ K}$) or the density drops significantly, which could be true at high altitudes or when the reconnection site migrates away. In the *former* case, the material bundle would correspond to the lower portion of a jet or surge, whose upper portion has upflows at reduced density and brightness. This gives rise to the diffuse appearance of the upper end of the bundle. This also explains why the streamlines of the falling material are distributed in a large volume and in various directions (Figure 13), not just along the path of the final collimated jet. This is because material is continuously ejected upward in different directions when the bundle

swings, as what happens when a fireman swings his firehose. In the *latter* case of reconnection site migration, the visible threads in the material bundle are constantly being replaced and we see different field lines over time as reconnection develops. This could explain why each sinusoidal oscillation (Figure 8) appears ephemerally.

As the system seeks its lowest energy state, the open-ended spine field line can change its orientation, while the null point migrates in space from field line to field line, depending on the dynamic evolution of reconnection (Figure 14). This seems to reflect what we observe here and explain the elbow (Figure 3) and the drift of the material bundle's lower end (Figure 13(c)). The latter is likely located near the null point and its overall upward migration may result from the upward development of reconnection as predicted in the standard flare model (Sturrock 1966; Kopp & Pneuman 1976) or from a cumulative effect of advection motions driven by gas pressure in the neighborhood of the null where the Lorentz force vanishes (Pariat et al. 2009). The low angle of the material bundle in its early stage probably reflects the strong horizontal field at low altitudes. The back-and-forth fast (151 km s^{-1} , see Figure 4 in Paper I) swing of the entire material bundle possibly results from catastrophic release of excessive twists into the open field, similar to the kink or writhe of a flux rope. Also, if we assume the measured twist propagation velocity 786 km s^{-1} to be the Alfvén velocity v_A , the velocity ratio $151/786 = 0.19$ is close to the 0.2 value of the drifting outer spine found in the 3D simulation of Pariat et al. (2009).

4.2. Discussion

Many characteristics of our observations and the above interpretation resemble those in the simulation of Török et al. (2009), particularly their fan-spine topology with a 3D null point resulting from emergence of a bipole into a locally unipolar region and the launch of a torsional MHD wave from the reconnection site. However, in their case, magnetic reconnection develops in two steps and each step leads to the formation of hot loops on each side of the spine, which constitute one half of a full anemone, consistent of the *Hinode* XRT observations of a specific jet event. In our case, we found no signature of such two-step reconnection, and we could not identify the expected inner spine emission (hatched with dashed lines in Figure 1(a)) in available data, presumably due to unfavorable temperatures and/or densities under the dome. However, the flare loop in SXR and EUV (Figures 13(g)–(h)) and its right branch in Ca II H (Figure 4(j)) are located in the expected position to the right hand side of the null point for the newly reconnected field.

We note that the upward expansion of the emerging flux toward the north has a large component *parallel* to the ambient field and can readily makes its way in a herniation manner, while the expansion toward the south must *perpendicularly* press the ambient field against strong resistance. This topological **asymmetry** can therefore preferentially facilitate the northward expansion, which is at least 4 times faster than its southward counterpart (Figure 10(f)). This is similar to the simulation of the primarily vertical (vs. horizontal) expansion of the dome in a vertical ambient field (Pariat et al. 2009). In addition, the null point can be more readily advected in the spine direction, as man-

ifested in its overall upward and northward migration (Figure 13(c)).

The northern leg starts to reverse its expansion and **retreat downward** at $t_4 = 02:51:44$ UT. In addition, when the material bundle sweeps toward the north, its lower end, assumed to be near the null point, slightly drops in height by $3''$ (Figures 10(d)). These occur near the peak of the flare, possibly when a significant amount of energy has been released. This is consistent with the implosion conjecture of Hudson (2000) and its theoretical demonstrations (Zhang & Low 2003; Janse & Low 2007). It predicts that after major energy release, the magnetic pressure (or energy density) in the local volume is significantly reduced and the resulting imbalance with the pressure in the surroundings would push this volume to contract. Observational evidence of this conjecture has gradually emerged (Liu et al. 2009a,c). When this happens, opposite to an expanding twisted flux rope in which twists tend to accumulate in the expanded top portion (Parker 1979, p. 189), more twists will be pushed by the Lorentz force to concentrate in the leg portion when the rope contracts. This explains why twists become more visible in the northern leg later when it contracts. This downward Lorentz force might also provide additional push to the material and help explain the faster than free-fall *downflow* observed here (Figures 11 and 12).

At the same time, some material is **ejected upward** at accelerations up to $(11.4 \pm 3.1)g_\odot$ (Figures 11 and 12). It is quite puzzling for this to take place simultaneously in the same northern leg as the fast downflow, even though they might occur on different field lines at separate line-of-sight positions. In any case, there are several possible explanations which we cannot distinguish with the available data: (1) If the ejection is on twisted field lines that reconnect with untwisted open field lines, it could be driven by the Lorentz force associated with the upward *relaxation* of twists, which seems to happen here (Figures 11(g)–(o)). (2) If the upward ejection and downflow are indeed on the same field lines, they could be the upward and downward branches of the secondary outflows bifurcated from the primary reconnection outflow as predicted in MHD simulations (Yokoyama & Shibata 1996; Moreno-Insertis et al. 2008). (3) Another less likely possibility is that the ejection and downflow are oppositely directed outflows from reconnection occurring at an X-point between them. An X-type null point at this location is, however, not favored by our adoption of the spine-fan topology to interpret this event.

The **disappearance of the Ca II H loop** possibly results from the combination of several processes, including mass drainage, temperature variation, and topological change. The first two mechanisms are expected to operate gradually, while the third one could happen catastrophically. First, as a flux rope emerges and plows through the lower atmospheres, dense material is dredged into the hot corona. Part of this material would contribute to the Ca emission seen at the fan surface. Such dense material is expected to be pulled back by **gravity** and slide down the dome, as seen in $H\alpha$ arch filaments (e.g. Chou & Zirin 1988). This is because the scale height of the $\lesssim 2 \times 10^4$ K plasma emitting the Ca II H line is only $\lesssim 1.2$ Mm and pressure gradient from gravitational stratification is simply too small to support the weight of

plasmas extending to the height of the dome (>10 Mm). In our case, such mass loss is evident in the northern leg of the loop. This would make the apex of the dome have the lowest density and become less well-defined and then invisible first, before the loop legs gradually fade away (Figures 10(e) and (f)). Second, **heating** of the Ca loop (fan surface) may occur during the course of its rise, possibly as a result of reconnection with the ambient field. Once its temperature rises above the $\lesssim 2 \times 10^4$ K range, the Ca II H loop would disappear. This can be seen in Figure 4(h), where the northern leg of the loop is vague in Ca but prominent and bright at 195 Å. Later, because of significant mass drainage that has considerably reduced the density of the loop (fan surface), it would no longer appear as detectable absorption or emission in EUV or SXR, as we see here (Figures 4(j)–(k)). Finally and more importantly, a catastrophic topological change, which may be involved in the launch of the chromospheric jet, can alter field connectivity and contribute to the disappearance of the fan surface in emission.

We note in passing that there is an **overarching loop brightening in SXR** at 02:44 UT (see Figure 4(b)) that appears simultaneously with the bright Ca II H loop (dark in EUV) but $\sim 10''$ higher in altitude. The southern leg of the Ca loop appears as dark absorption in SXR (Figure 4(f)), suggesting that the SXR loop brightening is located behind the Ca loop. When the legs of the Ca loop disappear around 02:55 UT (Figure 10(f)), this SXR loop becomes invisible too (Figure 4(j)). These timing coincidences seem to suggest that the SXR loop is of the same emerging flux system as the Ca loop but at higher altitudes and temperatures. However, during its lifetime, the SXR loop hardly changes its size or shape, while the Ca loop has risen more than $20''$, well beyond the XRT's $2''$ spatial resolution. This contradicts the expectation that the overarching SXR loop would expand together with the low lying Ca loop if they were of the same emerging flux system. Another possibility is that the SXR loop brightening represents heating during magnetic reconnection in a curved current sheet between the emerging and ambient fields, as suggested by Yoshimura & Kurokawa (1999) who found SXR brightening above emerging H α arch filaments. However, the location of the event within the inferred coronal hole poses a challenge for the existence of such a hot SXR loop as observed here. The nature of this transient SXR loop brightening thus remains an open question.

5. CONCLUSIONS

We have presented multiwavelength observations and detailed analysis of a chromospheric jet and its accompanying growing loop. This extends the study presented in Paper I which focused on the fine structure and kinematics of the jet itself. We summarize our new observations as follows.

1. Potential field extrapolation indicates that this event occurs in an equatorial **coronal hole** and as expected, the jet is closely aligned with the open field lines (Figures 5 and 6).
2. The predecessor of the jet is a **bundle of material threads** ($\lesssim 1''$ wide) extending from the chromosphere into the corona. This bundle exhibits

transverse **sinusoidal oscillations** across its axis, whose velocities range from 47 ± 9 to 58 ± 11 km s $^{-1}$, periods from 162 ± 11 to 197 ± 35 s, and amplitudes from 1.5 ± 0.3 to 1.7 ± 0.3 Mm. Such oscillations propagate upward at velocities as high as $v_{\text{ph}} = 786 \pm 30$ km s $^{-1}$ (Figures 8 and 9). We interpret these as evidence of propagating torsional MHD waves.

3. The material bundle first slowly and then rapidly swings up, with the orientation angle of its central axis from the limb growing by $>50^\circ$ in 10 minutes (Figure 10). The transition from the **slow to fast swing** phase coincides with the onset of an A4.9 flare, which heats the plasma to $T = 12.2 \pm 0.6$ MK. The bundle then swings back in a whiplike manner and develops into a collimated jet (Figure 3), which continues to exhibit transverse oscillations (see Paper I), but at fractionally slower rates than the earlier bundle mentioned above.
4. A **loop expands** simultaneously in these two phases. It attains a uniform vertical velocity of 16.2 ± 0.4 km s $^{-1}$ during the *gradual phase* and reaches 135 ± 4 km s $^{-1}$ at the end of the *acceleration phase* (Figure 10). The initial slow rise velocity is similar to those of emerging fluxes found in H α arch filaments and in MHD simulations. The lateral expansion is asymmetric and dominated by the northward displacement of the northern leg.
5. The loop appears to rupture or collapse near the peak of the flare and its apex becomes undetectable first. The northern leg of the loop **retreats downward** and material drains down to the photosphere at accelerations ($a = (-4.8 \pm 0.7)g_\odot$) greater than free-fall. At the same time, some material is **ejected upward** ($a = (11.4 \pm 3.1)g_\odot$) in the same leg (Figures 11 and 12; Section 4.2).
6. Some material falls back along streamlines in the original direction of ascent, showing no more transverse oscillations (Paper I). Most of the streamlines swerve around an inferred dome extending above the chromosphere and characterized with a null point at its top, depicting an **inverted-Y** geometry. These streamlines closely match in space the late Ca loop prior to its rupture, the X-ray flare loop, and the EUV absorption features (Figure 13).

We interpret (Section 4) these observations in the framework of the emergence of a twisted flux rope into an open field environment leading to the formation of a jet through magnetic reconnection (e.g., Heyvaerts et al. 1977; Yokoyama & Shibata 1995; Moreno-Insertis et al. 2008), and the relaxation of twists transferred into the jet leading to its spin (Shibata & Uchida 1985, 1986; Canfield et al. 1996; Török et al. 2009). We further identify signatures of the **fan-spine** topology throughout the event, from the precursor to post-eruption evolution. The *outer spine* is recognized as the *material bundle* that eventually develops into the *collimated jet*, while the *fan surface* is imaged as the *growing Ca loop* in projection. After the eruption, the presence of this magnetic skeleton is clearly implied by the streamline geometry of the falling material.

Our observations and model share commonalities with their counterparts in the literature, while the major differences given by our new findings are as follows.

1. The **simultaneous** growth of the emerging flux and development of the resulting jet, synchronized in two stages (Figure 10), have been clearly established here for the first time, to the best of our knowledge. Growing loops (other than post-flare loops) were recently noted in X-ray jet events (Shimojo et al. 2007; Chifor et al. 2008), but their detailed temporal evolution and relationship with the jet were not clear.
2. In previous models (e.g. Yokoyama & Shibata 1995), reconnection between the emerging flux and the overlying field would immediately lead to the launch of an eruptive jet. In our case, when the reconnection rate is *moderate* early in the event, the jet, manifesting itself as the material bundle, undergoes *quasi-static* evolution for more than 20 minutes. We call this an “**intermediate jet**” stage, which later develops into the classical *eruptive* jet as a result of *fast* reconnection driven by the accelerating expansion of the emerging flux. These are analogous to the slow and fast reconnections in the energy-storage and -release stages of coronal jet simulations, respectively (Pariat et al. 2010).
3. The whiplike motion of a jet has been predicted as a consequence of the sling-shot effect of the newly reconnected field lines (e.g., Shibata & Uchida 1985; Canfield et al. 1996), and has been observed as a *unidirectional* swing *away* from the accompanying flare where reconnection occurs. In our case, the axis of the material bundle **swings back and forth**, and the previously predicted whip motion

only applies to the second swing here when the material bundle moves into its collimated jet position. We interpret this as instabilities possibly related to the catastrophic unload of excessive twists (Section 4.1).

A statistical study of similar *Hinode* events is required before more general conclusions can be drawn. The validity of our phenomenological interpretation shall also be rigorously checked against theoretical models, numerical simulations (e.g., Pariat et al. 2010), and laboratory experiments (e.g., Bellan et al. 2005). Finally, as pointed out by Antiochos (1998), the emergence of a bipolar flux system in a unipolar region on the photosphere naturally produces a local minority-polarity region with a spine-fan helmet magnetic structure above it. Our observations clearly show such an event and have identified its observable dynamical characteristics, thus providing motivation for future investigation of the rich 3D magnetic topologies to be found in such structures.

This work was supported by *Hinode* SOT contract NNM07AA01C. *Hinode* is a Japanese mission developed and launched by ISAS/JAXA, with NAOJ as domestic partner and NASA and STFC (UK) as international partners. It is operated by these agencies in cooperation with ESA and NSC (Norway). We thank the anonymous referee for constructive comments and helpful suggestions. We are grateful to Paul Bellan, Marc DeRosa, Mark Cheung, Juan Martinez-Sykora, Yu Liu, Haimin Wang, Richard Shine, and Rita Ryutova for discussions and help of various kinds, to Yan Xu and Shuo Dai for help with YNAO H α data reduction, to Mei Zhang for comments on the manuscript, and to Dominic Zarro and William Thompson for help with *STEREO* maps.

REFERENCES

- Alexander, D. & Fletcher, L. 1999, *Sol. Phys.*, 190, 167
 Antiochos, S. K. 1998, *ApJ*, 502, L181
 Antiochos, S. K., DeVore, C. R., & Klimchuk, J. A. 1999, *ApJ*, 510, 485
 Archontis, V., Moreno-Insertis, F., Galsgaard, K., Hood, A., & O’Shea, E. 2004, *A&A*, 426, 1047
 Archontis, V., Tsinganos, K., & Gontikakis, C. 2010, *A&A*, 512, L2
 Asai, A., Shibata, K., Hara, H., & Nitta, N. V. 2008, *ApJ*, 673, 1188
 Battaglia, M., Fletcher, L., & Benz, A. O. 2009, *A&A*, 498, 891
 Bellan, P. M., You, S., & Hsu, S. C. 2005, *Ap&SS*, 298, 203
 Berger, T. E., et al. 2008, *ApJ*, 676, L89
 Brants, J. J. 1985, *Sol. Phys.*, 98, 197
 Brueckner, G. E. & Bartoe, J.-D. F. 1983, *ApJ*, 272, 329
 Bruzek, A. 1967, *Sol. Phys.*, 2, 451
 —. 1969, *Sol. Phys.*, 8, 29
 Canfield, R. C., Reardon, K. P., Leka, K. D., Shibata, K., Yokoyama, T., & Shimojo, M. 1996, *ApJ*, 464, 1016
 Chifor, C., Isobe, H., Mason, H. E., Hannah, I. G., Young, P. R., Del Zanna, G., Krucker, S., Ichimoto, K., Katsukawa, Y., & Yokoyama, T. 2008, *A&A*, 491, 279
 Chifor, C., Mason, H. E., Tripathi, D., Isobe, H., & Asai, A. 2006, *A&A*, 458, 965
 Chou, D. & Wang, H. 1987, *Sol. Phys.*, 110, 81
 Chou, D. & Zirin, H. 1988, *ApJ*, 333, 420
 Cirtain, J. W., et al. 2007, *Science*, 318, 1580
 Ding, J. Y., Madjarska, M. S., Doyle, J. G., & Lu, Q. M. 2010, *A&A*, 510, A111
 Ellison, M. A. 1944, *MNRAS*, 104, 22
 Fan, Y. 2009, *ApJ*, 697, 1529
 Fan, Y. & Gibson, S. E. 2004, *ApJ*, 609, 1123
 Filippov, B. 1999, *Sol. Phys.*, 185, 297
 Fivian, M., Hemmeck, R., McHedlishvili, A., & Zehnder, A. 2002, *Sol. Phys.*, 210, 87
 Fletcher, L., Metcalf, T. R., Alexander, D., Brown, D. S., & Ryder, L. A. 2001, *ApJ*, 554, 451
 Galsgaard, K., Moreno-Insertis, F., Archontis, V., & Hood, A. 2005, *ApJ*, 618, L153
 Golub, L., et al. 2007, *Sol. Phys.*, 243, 63
 Gouttebroze, P., Vial, J., & Heinzel, P. 1997, *Sol. Phys.*, 172, 125
 Handy, B. N., et al. 1999, *Sol. Phys.*, 187, 229
 Harvey, K. L. & Martin, S. F. 1973, *Sol. Phys.*, 32, 389
 Heyvaerts, J., Priest, E. R., & Rust, D. M. 1977, *ApJ*, 216, 123
 Hudson, H. S. 2000, *ApJ*, 531, L75
 Janse, A. M. & Low, B. C. 2007, *A&A*, 472, 957
 Jibben, P. & Canfield, R. C. 2004, *ApJ*, 610, 1129
 Kopp, R. A. & Pneuman, G. W. 1976, *Sol. Phys.*, 50, 85
 Kosugi, T., et al. 2007, *Sol. Phys.*, 243, 3
 Krucker, S., Hannah, I. G., & Lin, R. P. 2007, *ApJ*, 671, L193
 Kurokawa, H., Hanaoka, Y., Shibata, K., & Uchida, Y. 1987, *Sol. Phys.*, 108, 251
 Kurokawa, H. & Kawai, G. 1993, in *Astronomical Society of the Pacific Conference Series*, Vol. 46, IAU Colloq. 141: The Magnetic and Velocity Fields of Solar Active Regions, ed. H. Zirin, G. Ai, & H. Wang, 507
 Lau, Y. & Finn, J. M. 1990, *ApJ*, 350, 672
 Li, H., et al. 2007, *PASJ*, 59, 643
 Lin, R. P., et al. 2002, *Sol. Phys.*, 210, 3
 Liu, R., Wang, H., & Alexander, D. 2009a, *ApJ*, 696, 121

- Liu, W., Berger, T. E., Title, A. M., & Tarbell, T. D. 2009b, *ApJ*, 707, L37
- Liu, W., Petrosian, V., Dennis, B. R., & Holman, G. D. 2009c, *ApJ*, 693, 847
- Liu, W., Petrosian, V., Dennis, B. R., & Jiang, Y. W. 2008, *ApJ*, 676, 704
- Liu, W., Petrosian, V., & Mariska, J. T. 2009d, *ApJ*, 702, 1553
- Liu, W., Wang, T.-J., Dennis, B. R., & Holman, G. D. 2009e, *ApJ*, 698, 632
- Maclean, R. C., Parnell, C. E., & Galsgaard, K. 2009, *Sol. Phys.*, 260, 299
- Martínez-Sykora, J., Hansteen, V., & Carlsson, M. 2009, *ApJ*, 702, 129
- Masson, S., Pariat, E., Aulanier, G., & Schrijver, C. J. 2009, *ApJ*, 700, 559
- Milligan, R. O. & Dennis, B. R. 2009, *ApJ*, 699, 968
- Moore, R. L., Cirtain, J. W., Sterling, A. C., & Falconer, D. A. 2010, *ApJ*, 720, 757
- Moreno-Inertis, F., Galsgaard, K., & Ugarte-Urra, I. 2008, *ApJ*, 673, L211
- Morita, S., Shibata, K., Ueno, S., Ichimoto, K., Kitai, R., & Otsuji, K. 2010, *PASJ*, 62, 901
- Newton, H. W. 1934, *MNRAS*, 94, 472
- Nishizuka, N., Shimizu, M., Nakamura, T., Otsuji, K., Okamoto, T. J., Katsukawa, Y., & Shibata, K. 2008, *ApJ*, 683, L83
- Nitta, N. V., Mason, G. M., Wiedenbeck, M. E., Cohen, C. M. S., Krucker, S., Hannah, I. G., Shimojo, M., & Shibata, K. 2008, *ApJ*, 675, L125
- Ofman, L. & Wang, T. J. 2008, *A&A*, 482, L9
- Okamoto, T. J., et al. 2007, *Science*, 318, 1577
- Okamoto, T. J., et al. 2008, *ApJ*, 673, L215
- Pariat, E., Antiochos, S. K., & DeVore, C. R. 2009, *ApJ*, 691, 61
- . 2010, *ApJ*, 714, 1762
- Parker, E. N. 1955, *ApJ*, 121, 491
- . 1979, *Cosmical magnetic fields: Their origin and their activity*, ed. Parker, E. N.
- Patsourakos, S., Pariat, E., Vourlidas, A., Antiochos, S. K., & Wuelser, J. P. 2008, *ApJ*, 680, L73
- Rachmeler, L. A., Pariat, E., DeForest, C. E., Antiochos, S., & Török, T. 2010, *ApJ*, 715, 1556
- Roberts, Jr., P. H. 1970, PhD thesis, California Institute of Technology.
- Roy, J.-R. 1973, PhD thesis, University of Western Ontario
- Schrijver, C. J. & DeRosa, M. L. 2003, *Sol. Phys.*, 212, 165
- Shibata, K., et al. 1992, *PASJ*, 44, L173
- Shibata, K., et al. 2007, *Science*, 318, 1591
- Shibata, K. & Uchida, Y. 1985, *PASJ*, 37, 31
- . 1986, *Sol. Phys.*, 103, 299
- Shimojo, M., Hashimoto, S., Shibata, K., Hirayama, T., Hudson, H. S., & Acton, L. W. 1996, *PASJ*, 48, 123
- Shimojo, M., et al. 2007, *PASJ*, 59, 745
- Sterling, A. C. & Moore, R. L. 2005, *ApJ*, 630, 1148
- Strong, K. T., Harvey, K., Hirayama, T., Nitta, N., Shimizu, T., & Tsuneta, S. 1992, *PASJ*, 44, L161
- Sturrock, P. A. 1966, *Nature*, 211, 695
- Suematsu, Y., et al. 2008, *Sol. Phys.*, 249, 197
- Török, T., Aulanier, G., Schmieder, B., Reeves, K. K., & Golub, L. 2009, *ApJ*, 704, 485
- Tsuneta, S., et al. 2008, *Sol. Phys.*, 249, 167
- Waldmeier, M. 1937, *Zeitschrift für Astrophysik*, 14, 91
- Wang, Y.-M., et al. 1998, *ApJ*, 508, 899
- Weart, S. R. & Zirin, H. 1969, *PASP*, 81, 270
- Wuelser, J., et al. 2004, in *Society of Photo-Optical Instrumentation Engineers (SPIE) Conference Series*, Vol. 5171, Society of Photo-Optical Instrumentation Engineers (SPIE) Conference Series, ed. S. Fineschi & M. A. Gummin, 111–122
- Xu, A.-A., Yin, S.-Y., & Ding, J.-P. 1984, *Acta Astronomica Sinica*, 25, 119
- Yashiro, S. & Shibata, K. 2000, in *Astronomical Society of the Pacific Conference Series*, Vol. 205, Last Total Solar Eclipse of the Millennium, ed. W. Livingston & A. Özgüç, 133
- Yokoyama, T. & Shibata, K. 1995, *Nature*, 375, 42
- . 1996, *PASJ*, 48, 353
- Yoshimura, K. & Kurokawa, H. 1999, *ApJ*, 517, 964
- Zarro, D. M. & Lemen, J. R. 1988, *ApJ*, 329, 456
- Zhang, M. & Low, B. C. 2003, *ApJ*, 584, 479
- Zhao, X. & Hoeksema, J. T. 1994, *Sol. Phys.*, 151, 91
- Zwaan, C. 1978, *Sol. Phys.*, 60, 213

APPENDIX

A. IMAGE PROCESSING AND CROSS-INSTRUMENT COALIGNMENT

We describe below the procedures to process and coalign images obtained from *RHESSI*, *TRACE*, *Hinode* XRT and SOT, YNAO, and *STEREO* EUVI. The absolute solar coordinates of *RHESSI* images have sub-arcsecond accuracy owing to its limb sensing aspect system and star based roll angle measurements (Fivian et al. 2002). We thus used *RHESSI* images as a fiducial for our coalignment.

XRT images were processed using the `xrt_prep` and `xrt_jitter` routines. We selected three XRT images (at 02:50:49, 02:51:51, and 02:53:51 UT, exposure < 1 s) during the flare in which over-exposure was minimal. We then constructed three *RHESSI* images at 3–6 keV with 100 s integration centered at these times. Assuming these XRT and *RHESSI* emissions were from the same source at each time, we shifted the XRT image to match its centroid of the 99% brightness contour and that of the 50% contour of the corresponding *RHESSI* image. The averages of the required shifts at the three times are $\Delta x = 10''.3$ and $\Delta y = 11''.3$ in the solar west and north directions, respectively. By rotating the shifted XRT images about the *RHESSI* centroid to match the limb in a trial and error manner, we found that no additional rotation is needed and the y -axis is already the solar north.

To coalign *TRACE* 195 Å images, we noted that both *TRACE* and XRT observed flare loops except that XRT loops are hotter and located at slightly higher altitudes. We thus selected a pointing-corrected XRT image at 02:53:51 UT and a later *TRACE* image at 02:59:14 UT (when the hot XRT loops had cooled down) to match their flare loop legs. The *TRACE* image was required to be shifted by $\Delta x = -3''$ and $\Delta y = 14''$, and then rotated by 1° counter-clockwise about the centroid of the flare loop, $O = [975''.8, -42''.7]$, to match the limb.

For SOT observations, we first processed Ca II H images using the standard `fg_prep` routine with the `/no_pointing` option to disable automatic pointing correction which is currently not satisfactory. We then made relative coalignment by cross-correlating neighboring images. To find the absolute image coordinates, we noted that the $\lesssim 2 \times 10^4$ K Ca II H emitting plasma appeared as absorption in *TRACE* 195 Å images. We then selected a pointing-corrected *TRACE* image at 02:43:20 with a 65 s integration and summed the corresponding SOT images from 02:43:23 to 02:44:19 UT. By matching features including the jet material bundle, large spicules, and the limb, we found that the center of the SOT image must be placed at $x = 998''.9$ and $y = -32''.3$, and then the image should be rotated by 0.2° clockwise about point $O = [975''.8, -42''.7]$.

YNAO H α images were shifted and rotated to match the jet features in neighboring SOT images. *STEREO* EUVI images were processed using the `mk_secchi_map` routine that takes into account the pointing information of the spacecraft, with the `/rotate_on` option turned on to make the solar north the y -axis. We did not attempt to align images from EUVI and other instruments, since *STEREO* has a different distance and view angle to the Sun compared with the Earth view. Meanwhile, the two *STEREO* spacecraft were too close to allow for triangulation in 3D geometry at the time of the event.

The translation and rotation corrections found above were applied to all images from the corresponding instruments. The overall accuracy are $1''$ – $2''$ and $2''$ – $3''$ in the x and y directions, respectively.

B. *RHESSI* SPECTRAL ANALYSIS

To determine the temperature of the flare plasma, we fitted *RHESSI* X-ray spectra. Following Krucker et al. (2007), we used detectors 1, 4, and 6, which had suffered the least radiation damage by the time of this event (5 years after the launch) and had the best spectral resolution among the nine germanium detectors. We fitted the spectral data from each individual detector separately, averaged the fitting parameters among the three detectors to give the final result, and used their standard deviations as the uncertainties. Details of this procedure were described in Liu et al. (2008) and Milligan & Dennis (2009). Figure 15 shows the spectrum at the peak of the flare, which is best fitted with an isothermal model and yields a temperature of $T = 12.2 \pm 0.6$ MK and emission measure of $EM = (5.3 \pm 0.5) \times 10^{45} \text{ cm}^{-3}$. There is pronounced ion line emission at 6.7 keV and no signature of nonthermal emission.

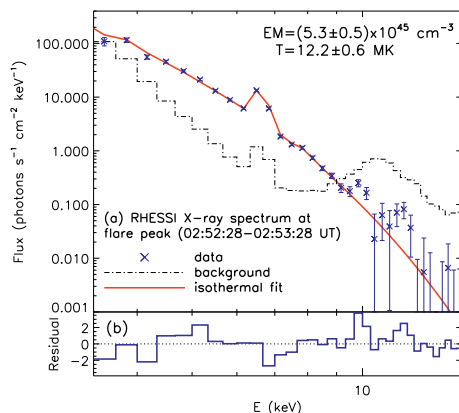


FIG. 15.— (a) Spatially integrated *RHESSI* X-ray spectrum at the peak of the flare, averaged among detectors 1, 4, and 6 and fitted with an isothermal model. (b) Fitting residuals normalized to the 1σ uncertainty of the measured flux at each energy.

C. NATURE OF Ca II H EMISSION DISPLACEMENTS

The resonance H line emission of Ca II ions has contributions from scattering of photospheric radiation and from thermal emission (collisional excitation). In general, the former decreases with temperature because of progressive ionization and the latter increases with temperature because of increased collisional rates. The emission decreases sharply with temperature when $T \gtrsim 2 \times 10^4$ K (Gouttebroze et al. 1997).

Based on the following reasonings, we believe that the displacements of Ca emission features presented in this paper primarily result from mass motions rather than sequential excitations of emission due to temperature or density variations. The Ca II H line emitting plasma has typical temperatures of $\lesssim 2 \times 10^4$ K, which is in the temperature range of the chromosphere. The Ca material bundle and loop also first appear at spicule heights in the chromosphere and then develop upward. This suggests a chromospheric origin of the material that is likely of high density as a result of flux emergence discussed in Section 4. In addition, such features are no weaker in Ca II H emission and in 195 \AA absorption than the nearby prominence (Figure 4) at similar temperatures. This prominence, clearly visible in AR 10940 through its entire disk passage (<http://www.solarmonitor.org/index.php?date=20070206>), is now just behind the limb and in the background of the event. Assuming that they have comparable line-of-sight extents, the density of the prominence, which has typical values of 10^{11} – 10^{12} cm^{-3} , provides a lower limit for the density in the Ca material bundle, loop, and jet. This inference has two implications: (1) the temperature of the dense, cool material distributed in such an extended volume (cf., the compact flare site) is not expected to change rapidly because of its large heat capacity, and thus the motions of these Ca emission features are unlikely a result of sequential temperature variations on such short time scales of ~ 10 s; and (2) more importantly, these features are two orders of magnitude denser than the ambient corona, and thus their motions are unlikely a consequence of sequential compression of coronal plasma either. Moreover, compression would heat the million degree coronal plasma to even higher temperatures that are further away from the Ca II H emission regime of two orders of magnitude cooler. For comparison, in an MHD experiment (Pariat et al. 2009), the compressional density enhancement responsible for supplying mass to a jet from a coronal origin is merely a factor of two.